Hydration forces between aligned DNA helices undergoing B to A conformational change: in-situ x-ray fiber diffraction studies in a humidity and temperature controlled environment

Ryan Case [a], Hauke Schollmeyer[a], Phillip Kohl [b], Eric B. Sirota [c], Roger Pynn [d], Kai E. Ewert [a], Cyrus R. Safinya [a,*], Youli Li [b,*]

[a]Materials, Physics and Molecular, Cellular and Developmental Biology Departments, University of California at Santa Barbara, CA 93106

[b]Materials Research Laboratory, University of California at Santa Barbara, CA 93106

[c]Corporate Strategic Research, ExxonMobil Research and Engineering Co., Annandale, NJ 08801

[d]Department of Physics and Indiana University Cyclotron Facility, Indiana University, Bloomington, IN 47408

[*]Authors to whom correspondence should be addressed. E-mail addresses: YOULI@MRL.UCSB.EDU and SAFINYA@MRL.UCSB.EDU

ABSTRACT

Hydration forces between DNA molecules in the A- and B-Form were studied using a newly developed technique enabling simultaneous in situ control of temperature and relative humidity. X-ray diffraction data were collected from oriented calf-thymus DNA fibers in the relative humidity range of 98%-70%, during which DNA undergoes the B- to A-form transition. Coexistence of both forms was observed over a finite humidity range at the transition. The change in DNA separation in response to variation in humidity, i.e. change of chemical potential, led to the derivation of a force-distance curve with a characteristic exponential decay constant of ~ 2 Å for both A- and B-DNA. While previous osmotic stress measurements had yielded similar force-decay constants, they were limited to B-DNA with a surface separation (wall-to-wall distance) typically > 5 Å. The current investigation confirms that the hydration force remains dominant even in the dry A-DNA state and at surface separation down to ~1.5 Å, within the first hydration shell. It is shown that the observed chemical potential difference between the A and B states could be attributed to the water layer inside the major and minor grooves of the A-DNA double helices, which can partially interpenetrate each other in the tightly packed A phase. The humidity-controlled x-ray diffraction method described here can be employed to perform direct force measurements on a broad range of biological structures such as membranes and filamentous protein networks.

KEYWORDS: Hydration force, DNA phases, DNA fibers, in-situ x-ray diffraction, humidity and temperature control

I. Introduction

Temperature and hydration are two important environmental variables affecting the structure of biological molecules, many of which undergo phase transitions as a function of relative humidity and temperature. A particularly well-studied example is the distinct conformational changes of the DNA double helix induced by varying relative humidity. In their very early work on partially dehydrated DNA fibers, Franklin and Gosling first identified two distinct (i.e. B and A) forms of DNA at different relative humidity based on x-ray fiber diffraction patterns (Franklin & Gosling, 1953a,b). High salt conditions or special nucleotide sequences could lead to the formation of left-handed Z-DNA (Mitsui et al., 1970; Berg et al., 2002).

In addition to changes in the molecular structure of the DNA double helix, the interaction between DNA molecules, mediated by water molecules and/or ions, leads to rich mesophases spanning from isotropic to 2D hexagonal and ultimately full 3D crystalline order in concentrated solutions (Durand et al., 1992 ; Fuller et al., 2004; Livolant et al., 1989 ; Livolant and Leforestier, 1996). The sensitivity of the DNA structure to humidity is a clear manifestation of the intimate interaction of water with the internal structure of DNA. High-resolution crystallographic studies on single crystals of oligo-DNA molecules confirmed the presence of a "water-ribbon" winding through the minor grooves of the DNA double helix, and the water molecules within the DNA were shown to be highly localized within the first hydration shell (<3 Å thickness) (Egli et al., 1998; Guerri et al., 1998). These oriented water molecules form complex patterns that could extend as far out as the fourth hydration shell and have been hypothesized to play some role in sequence recognition (Chaplin, 2006).

The interaction of overlapping hydration layers of different DNA molecules contributes to the stabilization of a lattice via a repulsive hydration force. This force, which decays quasi-exponentially with separation distance, in effect resists the removal of water between closely packed DNA molecules. Hydration forces have been observed experimentally in a number of systems consisting of polar surfaces and linear molecules (Leikin et al., 1993; Parsegian and Zemb, 2011). The force-distance curves in all these systems exhibit remarkably similar exponential decay lengths, suggesting a common origin underlying these forces. A full and complete theoretical understanding of the hydration force has not yet emerged. It is generally accepted, however, that the force results from the summation of weak forces related to small perturbations of large number of water molecules by the macromolecules or surfaces (Parsegian and Zemb, 2011).

Previous measurements on DNA hydration forces have been performed by measuring DNA lattice constant change in response to osmotic pressure induced by mixing colloidal molecules with DNA in solution (Parsegian and Fuller, et al., 1979; Rau et al., 1984; Rau and Parsegian, 1992). Due to experimental limitations these measurements had been performed only for B-DNA with surface separation typically > 5 Å. Here we describe a new technique enabling simultaneous temperature and hydration (relative humidity) control in a sample environment suitable for both small- and wide-angle x-ray scattering (SAXS and WAXS) studies of soft-condensed matter and biological systems. The technique was employed to collect in-situ X-ray diffraction data from oriented DNA fibers at precise relative humidity intervals, with DNA molecules in either the B or A conformational states, and during the B to A transition. The data enabled derivation of the hydration force curve in the previously un-probed surface separation

range of ~1.5 Å to 6 Å and for DNA in either A- or B-form. It was necessary to consider the contribution of water within the major and minor grooves of A-DNA at separations < 2.5 Å.

2. Development of the compact temperature and humidity chamber for in-situ x-ray diffraction

2.1 Design principle

Two techniques have been widely used in humidity controlled measurements: mixing streams of water vapor with dry air (Fuller et al., 2004; Sirota et al., 1988; Smith et al., 1990) and using reservoirs filled with saturated salt solutions to regulate vapor pressure/humidity (van Dam et al., 2002; Franklin and Gosling, 1953; Langridge et al., 1960). Both techniques suffer some drawbacks. The water vapor and air mixing scheme requires sample chambers that are typically bulky and consequently cumbersome to use. The saturated salt solution technique provides only discrete control in humidity levels and generally lacks a high degree of accuracy. In addition, salt-induced corrosion leads to degradation of the chamber. Here a unique design is presented that uses a temperature differential between the sample and a water bath, both of which are contained in a sealed chamber to control the relative humidity. This simple design results in a compact, self-contained apparatus that can be mounted on a variety of XRD instruments with laboratory and synchrotron radiation for in-situ humidity/temperature (H/T) controlled studies.

The working principle of the in-situ H/T chamber is based on independent and precise control of two temperature points within the sample environment. As schematically shown in Fig. 1a, the chamber consists of a sealed and thermally insulated cylindrical shell connected to a water reservoir (bath) via a small opening at the base (Sirota and Wu, 1996). The sample is suspended in the center of the sealed chamber. The water bath is thermally insulted from the

sample shell, which enables independent control of the temperatures of the sample cell (T_1) and the water bath (T_2). The temperature of the water bath sets the dew point of the sample environment within the sealed housing, and hence the water vapor partial pressure, and from that the relative humidity can be calculated as follows. The dew point of the sample environment (T_2) sets the partial pressure of water vapor at the sample $P(T_2)$. The relative humidity of an environment is defined as the ratio of the amount of water vapor present to the amount of water vapor that can be held at T_1. Assuming that water vapor acts as an ideal gas, this ratio is equivalent to the ratio between the partial pressure of water vapor present to the partial pressure of water vapor in a saturated environment. Hence:

$$\%RH = 100\% * \frac{P(T_2)}{P(T_1)} \quad (1)$$

where T_2 is the dew point temperature, which is equal to the water bath temperature, T_1 is the sample temperature, and $P(T_1)$ is the partial pressure of saturated water vapor at T_1. When T_1 is at or below T_2, the sample is fully hydrated (RH=100%), whereas for $T_1 > T_2$, the sample will always be at partial humidity (RH<100%). By varying T_1 and T_2 one can set both the temperature and humidity for the sample at precise increments, which makes this technique very useful for in-situ experiments.

Phase transitions that occur at constant temperature and pressure, such as the transition from liquid to vapor, also occur at a constant free energy, i.e. $\Delta G(P, T) = 0$, when the system is in equilibrium. Under this condition, the vapor pressure is related to temperature via

$$\left(\frac{\partial p}{\partial T}\right)_{\Delta G} = \frac{\Delta H}{T \Delta V} \quad (2)$$

where ΔH is the change of enthalpy of the transition, which is the molar latent heat of vaporization, T is the temperature of the transition, and ΔV is the change of volume of the

substance. In the liquid to vapor transition, ΔV is approximately the volume of the vapor since the vapor volume is much larger than the liquid volume. Assuming that ΔH is approximately independent of temperature T, the partial pressures of saturated water vapor at any temperature can be described by the Clausius-Clapeyron Equation (Haar et al., 1984):

$$P(T) = P_0 \, e^{-\frac{\Delta H_{vap}}{RT}} \qquad (3)$$

where P_0 is a constant, ΔH_{vap} is the molar latent heat of vaporization of water, R is the ideal gas constant, and T is the absolute temperature. Fig. 1b shows the results of the fit to tabulated P(T) values using the Clausius-Clapeyron equation (Haar et al., 1984). Because it is assumed that the latent heat of vaporization of water ΔH_{vap} is constant with respect to temperature, there is a minor deviation from the tabulated data. However, for the purposes of the experimental setup, this error is considered negligible compared to other experimental variables, such as temperature accuracy and uniformity. In the experiments to be presented, the vapor pressures were calculated by linearly interpolating between two points of the tabulated curve.

The range of relative humidity that can be achieved with the chamber is dependent on temperature. The practical range of operation (RH vs T), calculated using equations (1) and (3), is shown in Fig.1 c. Although the principle described above can be applied to other solvents, for practical purposes we will only consider the range using water. The temperature range is set to be sufficiently above the freezing point and below the boiling point of water (10 ^{o}C - 95 ^{o}C). The controllable range of RH increases at higher temperatures. At a sample temperature of 25 ^{o}C, the achievable range of RH is 27.5%-98%. At 75 ^{o}C, the range is 2.3% - 98%. It should be noted there are significant challenges for RH values > 95%, due to the very small temperature difference between the sample and the water reservoir.

2.2 Sample Chamber Design

The mechanical design of the H/T chamber is illustrated in Fig. 2a. Good temperature stability is crucial to achieving precise humidity control. Thus the sample chamber consists of three concentric hollow cylinders (shells): the inner two made of aluminum and the outer shell made of plexiglas, which is not shown in the figure. The plexiglas outer shell acts merely as a thermal jacket, shielding the inner two cans from ambient air currents. The two aluminum cylinders are supported on a Teflon insulator, underneath which lies the water bath container. The water bath is heated or cooled to the desired dew point by a Peltier device mounted on an aluminum plate, which is used as both a support on the sample stage and a heat exchanger to draw excess heat away from the system. A Teflon spacer is placed between the water bath base and the aluminum cylinders to provide thermal insulation between the water bath and the ambient sample environment. A 0.5 inch (12.7mm) opening in the center of the spacer allows the water vapor to enter the sample chamber from the water bath.

To minimize x-ray attenuation, the inner cylinders are sealed with aluminized Kapton windows, and the plexiglas cylinder is covered with Mylar windows. However, x-ray scattering from the polymer windows exhibit a ring-like pattern, which could obscure the features of interest. To eliminate this parasitic background, small pass-through holes (~3mm in diameter) are punched through the windows at the beam position after the sample to prevent the intense direct beam from striking the windows. To seal the sample chamber, the through holes are covered with 4 μm thick pieces of aluminum foil. The thin aluminum foil is used because 1) it only negligibly attenuates the beam (~5%), and 2) its scattering signal is outside the region of interest for most biological systems and therefore does not contribute significantly to the

background. The scattering signal from the windows on the incident beam side of the chamber is blocked by an aperture placed just before the sample.

The control diagram for the chamber is shown in Fig. 2b. Resistive heaters are used to heat the ambient sample environment. The temperatures of the outer aluminum cylinder (sample chamber) and the water bath are controlled by two separate Wheatstone bridge circuits with YSI model 44011 thermistors as the control sensor. The resistive heaters used for the ambient sample environment and the Peltier plate used for the water bath are powered by two separate power supplies, one for each control circuit.

The temperature of the sample T_{sample} is controlled by setting the temperature of the outer aluminum cylinder $T_{cylinder}$, and influenced to a small degree by the temperature of the water bath $T_{reservoir}$. Because T_{sample} and $T_{reservoir}$ can be independently controlled, for the most part, there is a vertical temperature gradient from the reservoir to the sample. Furthermore, the low thermal conductivity of the aluminized Kapton windows can lead to non-uniform temperature on the outer aluminum cylinder and water condensation on the interior surfaces of the windows at high humidity levels. In such cases, additional heaters are necessary for the windows.

To account for such temperature gradients, three independent thermistors are used to monitor the temperatures of the sample, the outer aluminum cylinder surface, and the water bath, respectively; hence, a total of five temperature sensors are used in this chamber. The thermistors used have an absolute accuracy of $\pm 0.2\ ^{o}C$. Applying the Clausius-Clapeyron Equation to relate the relative humidity to the independent water bath and sample temperatures, the corresponding absolute accuracy of relative humidity in the range of 65% or more is about ±2%. The temperature control stability is better than $0.01\ ^{o}C$, implying a relative humidity stability of ~0.1%.

2.3 Calibration

To calibrate the H/T chamber, the phase behavior of a freely suspended sample of the phopholipid 1-2-dimyristoyl-*sn*-glycero-phosphatidylcholine (DMPC) was investigated and compared with published results measured with conventional vapor mixing method (Sirota, et al., 1988; Smith, et al., 1988; Smith, et al., 1990). It is well established that DMPC forms two distinct lamellar phases at temperatures above 30 °C: L_α and $L_{\beta F}$. As shown schematically in Fig. 3c and 3d, respectively, the L_α phase is a lamellar phase in which the chains are fluid-like, whereas the $L_{\beta F}$ phase displays ordered chains. At a given temperature, it is known that DMPC undergoes a phase transition from L_α to $L_{\beta F}$ with decreasing relative humidity. This phase boundary was used as a reference for calibrating the chamber.

The structural transition from L_α to $L_{\beta F}$ is evident in the 2D x-ray diffraction data (Fig.3a and b), which was collected from the DMPC sample at the same temperature (36.6 ^oC) but at two slightly different RH levels near the phase boundary (70.4% and 69.4% RH, respectively). The data shows two sets of peaks corresponding to ordering along different molecular orientations: A series of sharp, roughly equally spaced, centro-symmetric arcs along the meridian represents the (00L) harmonics of the lamellar stacking of the lipid molecules, whereas in the equatorial direction, at much larger q (smaller spacing) the correlations between the alkyl tails gives rise to a broad arc of scattering intensity.

The difference between the two diffraction patterns becomes even more evident in projection scans along and perpendicular to the lamellar stacking direction, shown in Fig. 4e and f, respectively. Both the lamellar peaks and the chain-chain correlation peak sharpened as the relative humidity was reduced, indicative of the transition to the more ordered $L_{\beta F}$ phase. Due to

the diffusion-limited variation of humidity within the thickness of the sample, there is evidence of coexistence of L_α and $L_{\beta F}$ domains in the data at lower humidity, as indicated by splitting of the lamellar peaks. As the lipid transitions from the L_α phase to the $L_{\beta F}$ phase, the lamellar spacing increases because the chains elongate as they lock into the ordered state, leading to a progressively larger shift of higher-order harmonics toward lower scattering angles. The design of the new H/T chamber was validated by the fact that the measured L_α to $L_{\beta f}$ phase boundary (RH ~69.8%) was in good agreement with published data obtained with conventional vapor mixing humidity control (Smith et al., 1990).

3. In-situ X-Ray diffraction studies of oriented DNA fibers

The H/T chamber was employed to study the hydration forces of oriented DNA molecules via in-situ humidity-controlled x-ray fiber diffraction. It is well known that DNA (the Na salt) undergoes a phase transition from the B-form to the A-form at 75% relative humidity at room temperature (Franklin and Gosling 1953a,b; Fuller et al., 1965). The B-form, the structure of which was first elucidated by Watson and Crick (Watson and Crick, 1953), is a double helix structure with a pitch of 34 Å, diameter of 20 Å, and vertical rise of 3.4 Å per base pair. The A-form is a double helix with a pitch of 28 Å, diameter of 23 Å, and rise per base pair of 2.6 Å (Pattabhi and Gautham, 2002). Because of the high precision of determining molecular separation from its well-characterized x-ray diffraction pattern, DNA has been extensively used as a model system for studying hydration forces. The majority of the experiments had been carried out by using the osmotic stress technique combined with x-ray diffraction in the relatively dilute regime in which the DNA molecules were separated by more than 5 Å of water (Parsegian et al., 1979; Rau et al., 1984; Rau and Parsegian, 1992). The DNA molecules were

believed to be in the B-form and were in general considered to be smooth, solid rods separated by water. This simple model underpins the majority of force-distance-analysis so far. It is unclear, however, whether the same hydration force relationship holds true for A-DNA, which exists at much lower humidity. In addition, crystallographic studies of oligo-DNA molecules have established that the DNA double helix holds a considerable amount of water in its grooves (Egli et al., 1998; Guerri et al., 1998), which would argue against modeling DNA as smooth rods. The current study aims to elucidate these effects with in-situ measurements at precise humidity intervals and at much smaller DNA separation (~1.5 Å – 6 Å) than previous studies. It is expected that in this regime, the assumption that the DNA molecules are smooth rods is no longer valid and one must consider the structural details within the grooves of the DNA to interpret the hydration force data.

For filamentous molecules, the quality of diffraction data improves with increasing degree of alignment. An in-situ fiber puller was constructed to produce aligned DNA fibers for H/T studies in the cell, based on the method first described by Franklin and Gosling (Franklin and Gosling, 1953a,b). This technique has also been widely used to align discotic liquid crystals (Safinya et al., 1984, 1985). The puller shown in Fig. 4a consists of a cup containing the DNA solution and a moving pin. The DNA solution used to draw the fibers consisted of 40 weight% Calf Thymus DNA and 60 weight% buffer, a 100 mM solution of KCl. At this concentration, DNA forms a columnar hexagonal phase and is most conducive to growing fibers (Blanc et al., 2001; Livolant et al., 1991a,b). The speed at which the fiber is drawn directly influences the size and quality of the fiber and is controlled by using a computer-controlled step motor. A typical fiber was about 5 mm in length, and between 300μm and 500μm thick. The fiber, intact on the fiber puller assembly, was next placed in the humidity-controlled chamber and was left to

equilibrate for at 1 to 20 hours before x-ray data was taken. Each fiber was viewed under polarized microscopy to check for alignment. Fig.4b and c show optical microscopy images of a DNA fiber viewed under crossed polarizers (The sample was rotated 45 degrees in the two images). The dramatic difference in brightness confirms the presence of strong birefringence due to alignment of the highly anisotropic DNA molecules. It is evident that the fiber actually consisted of a bundle of smaller, more crystalline micro-fibers that are axially aligned. The orientation of the micro-fibers in the direction perpendicular to fiber axis is random, thus giving rise to a diffraction pattern equivalent to the rotationally averaged diffraction pattern from a single crystal fiber.

A series of 2D x-ray diffraction patterns collected in-situ from an aligned DNA fiber inside the H/T oven at different humidity levels is shown in Fig.5. It is worth noting that the experiments were performed on a single fiber sample typically over a period of several days, sometimes with very small humidity level changes in between measurements. The diffraction data shown is representative of more than 10 sets of repeat measurements. The striking "X"-shaped scattering feature, most obvious in the top four panels, is characteristic of the helical structure of DNA in the B-form (Franklin and Gosling, 1953a,b; Atkins, 1994). As the humidity level decreases below 87%, the diffraction feature of the A-form appears. Between 82.7%-86.7% RH, the diffraction data is a superposition of both A- and B-forms, indicating co-existence. At RH < 80%, the structure is pure A-form, which is characterized by much more crystal-like diffraction patterns.

Equatorial peaks in the diffraction data are consistent with hexagonal packing of DNA molecules in the plane normal to the helical axis. In the data for the B-form, the helical layer lines are the main features, indicating that the neighboring DNA molecules lack correlation in

the longitudinal (axial) direction. Thus, it is likely that the B-form DNA molecules are in the hexagonal columnar phase, with molecules free to slide past each other (Livolant et al., 1989). In comparison, the data for A-form DNA at lower humidity levels show distinct spots that are consistent with a "lattice" type of arrangement in which the neighboring DNA molecules are registered in both the longitudinal and lateral directions. Even though the DNA helices are more ordered in this phase (with density correlation between neighboring molecules), it cannot be considered a 3D crystal, since there is no specific base-pair to base-pair locking because of sequence variation. As we show later (in section 4.2), these molecular packing details have important implications when the hydration force curve is derived from the diffraction patterns.

4. Discussions

4.1 B to A form transition

The transition from B-form to A-form is examined by plotting the change of the double helix pitch as a function of relative humidity. As shown in Fig.6a, the onset of the transition from B- to A-form occurs at ~87% RH within a narrow range (~0.3% RH) and is discontinuous. At RH between 82.7% and 86.7% (vertical dashed lines), there is evidence of coexistence of B and A forms in the diffraction data. In the mixed phase diffraction data, it was possible to extract the pitch parameters for both forms, which are plotted on the same curve using different symbols. At RH<80%, the signatures of the B-form are no longer detectable. The absence of any diffraction signature other than that from B- and A-form DNA during the transition confirms that there are no intermediate states between the B- and A-form. Thus, the B to A conformational change can be considered as a first order phase transition (Fuller et al., 2004). This result is consistent with previous experimental measurements and also with more recent molecular dynamics studies (Banavali and Roux, 2005; Dickerson and Ng, 2001; Fuller at al., 2004). It should be noted that

although it is expected that the transition is fully reversible, the experiments described here were only conducted along the path from high to low RH.

4.2 Hydration force in DNA

The humidity-driven structural changes in the DNA fiber have been used as a model system to study the hydration force between linear molecules. The removal of water through the drying process, i.e. the reduction of the relative humidity costs energy due to the change in the chemical potential of the water vapor. This change in chemical potential can be calculated from the relative humidity as shown by Parsegian and others (Parsegian et al., 1979; Smith et al., 1988, 1990) as:

$$\Delta\mu = RT \ln(P_{water\text{-}vapor}/P_{saturation}) = RT \ln(RH) \quad (4)$$

where $\Delta\mu$ is the change of the chemical potential in a mol volume of water vapor, R is the ideal gas constant, T is the absolute temperature, and RH is the relative humidity of the environment. $\Delta\mu$ has the unit of energy (work) per unit volume (e.g. ergs / cm^3) but can also be expressed as a differential pressure or force per unit area: dyne/cm^2 by using the relation 1 erg = 1 dyne cm. Thus, the change in chemical potential is directly related to the hydration force, which is believed to be the dominant force maintaining the DNA rod-to-rod separation. The microscopic origin of this force is not fully understood (Parsegian and Zemb, 2011; Podgornik et al., 1994). It is known, however, to have an exponential dependency on the distance between DNA molecules of the form (Parsegian et al., 1979; Smith et al., 1988, 1990): $f_{hyd} \sim e^{-d_w/\lambda}$, where d_w is the thickness of the water layer between DNA molecules and λ is the hydration force decay constant.

To extract the relevant force-distance curve from the data, the equatorial peaks in the fiber diffraction patterns were used to determine the axial spacing (separation) between the DNA

molecules. A hexagonal packing model was used to index the peaks, resulting in a single lattice parameter *a* (interhelical spacing) that describes the axial separation (center-to-center) between neighboring DNA molecules in the plane perpendicular to the fiber axis. Since we are concerned with only equatorial reflections, the lattice parameter can be derived from the measured d-spacing of the first peak $d_{(1\ 0\ 0)}$ by the equation $a=2d_{(1\ 0\ 0)}/\sqrt{3}$. In the B-form, this hexagonal packing model is well accepted. Here this model also works well for A-form equatorial data and can be justified as follows. A crystallographic indexing of the A-form data requires a c-centered monoclinic lattice (Fuller, 1965). However, since the hydration force is interpreted only in terms of rod-to-rod distance, we need to concern ourselves only with in-plane packing (i.e. average interhelical spacing). Thus the monoclinic cell reduces to a centered 2D rectangular cell. The in-plane lattice constants *(a,b)*, which vary with hydration and ionic strengths, are generally quite close to being hexagonal with $a/b \sim \sqrt{3}$. Additionally, the true crystalline A-form only manifests at the very low end of humidity (<80%) in the current study. Considering that the fiber sample is composed of multiple micro-fibers, we must also take into account rotational averaging in-plane. Taken together, these effects justify using a simpler hexagonal indexing scheme to calculate the isotropic axial separation between DNA rods in the fiber sample even in the A-phase.

The intensity profiles of the first equatorial peak at several RH points near the B- to A-form transition are shown in Fig.6b. At RH=88.6%, the sample is in the B phase in which all DNA are in the B-form. The (1 0 0) hexagonal peak is sharp and has high intensity. At RH=82.7%, the majority of the DNA in the sample is in the A-form (A phase). The peak, which is taken as the (1 0 0) peak in the pseudo-hexagonal lattice, is broader and weaker. In between these two RH values, the system undergoes the B- to A-form transition with co-existence of both forms, with the percentage of A phase increasing as RH is lowered. It is interesting to note that

during the transition the (1 0 0) peak position remains unchanged, indicating a fixed axial separation between DNA molecules either in the A- or B-form, while the peak intensity gradually decreases.

The hydration force curve derived from the DNA fiber diffraction data as a function of humidity is shown in Fig.7. The force (in log scale), represented as a change in chemical potential per unit volume (ergs/cm^3), which is equivalent to a differential pressure (dyne/cm^2, force per unit area), is plotted against DNA interhelical spacing *d*. For hexagonal packing, *d* is equal to the 2D hexagonal lattice constant *a*. Two features stand out in the graph and merit further discussion. First, it can be seen that the data points fit well to straight lines both in the A and B phases, as expected due to the exponential dependence of the hydration force vs separation. The slopes of the two lines, which are described as force decay constants (λ), are 1.96 Å and 1.94 Å, for A- and B forms of the DNA, respectively. The difference in the decay lengths in the two forms is within experimental uncertainty and both values agree well with the generally accepted decay constant of ~2 Å found in a large number of systems studied previously (Parsegian and Zemb, 2011).

The high concentration of DNA (and fairly high salt concentration) in the sample resulted in measured axial separation ranging from 21.8 Å – 25.3 Å. As shown in Fig. 7, the B-form to A-form conversion starts at an axial separation of d_{AB} = 23.4 Å, which remains constant through the transition. This particular axial spacing at which both A- and B-form DNA co-exist is meaningful in two ways. First, if we subtract the diameter of B-DNA (20 Å) from d_{AB}, we find that the surface separation for B-DNA is equal to 3.4 Å, indicating that neighboring B-DNA are within one hydration shell of each other. Second, it is perhaps no coincidence that d_{AB} is only slightly larger than the diameter of A-DNA (23 Å). This suggests that at even lower humidity

(i.e. smaller axial separation), in the A phase there is interpenetration of the DNA helices. The fact that force decay constant in both the A and B phase is essentially the same suggests that hydration force continues to play a dominant role in maintaining DNA rod-to-rod separation even in the tightly packed, and much drier A phase.

The second noticeable feature in Fig. 7 is the vertical shift in the force curves for A and B phases. This shift (chemical potential change) is related to the fact that the A-DNA and B-DNA are in different free energy states (Banavali and Roux, 2005). Since the hydration force curves in both A and B phases have the same force decay constant (~2 Å), it is reasonable to assume that the same force-distance relationship also holds during the B to A transition. Thus, using the same exponential formula one could model the vertical shift of the force curve in the A phase by an effective reduction in water layer thickness Δd_w as

$$\Delta d_w = (d_A - d_B) + \lambda[\ln(-\Delta\mu_B) - \ln(-\Delta\mu_A)] \quad (5)$$

Where d_A and d_B are the diameters of A- and B-DNA, respectively, λ=2 Å is the force decay constant, $\Delta\mu_B$ and $\Delta\mu_A$ are the chemical potential values corresponding to the onset of pure B and A phases, respectively (end points on the vertical rise in the transition regime). Based on data shown in Fig. 7, a Δd_w value of 2.4 Å was obtained. The significance of this value will become evident in discussions below.

To examine the hydration force in the A and B phases, it is necessary to derive the actual water layer thickness values upon which the hydration force depends ($f_{hyd} \sim e^{-d_w/\lambda}$). Generally this is done by converting the axial spacing d into wall-to-wall separation d_w by substracting the diameter of the DNA double helix. For the B phase, this method produces reasonable values, however for the A phase it results in non-physical negative distances since the interhelical separation can be smaller than the diameter of A-DNA. This suggests that there is

interpenetration of the helices in the A phase and we must derive d_w using a different approach. To do this, we shall consider the difference in packing between the A- and B-forms of DNA and its consequences in hydration force calculation.

It is important to realize that the measured "hydration force" is actually the net summation of all the work related to removing water from the system. Considering the hexagonal packing of DNA, one realizes that there is actually a whole range of d_w (wall-to-wall separation or water layer thickness) in the structure. However, due to the exponentially decaying nature of the hydration force, the dominant contribution would come from parts of the structure where d_w is small. In other words, it is essential to define the minimal separation (water layer thickness) in the structure. In the B-form, the DNA molecules are able to slide in the axial direction (columnar hexagonal packing). This effectively averages the density over the entire length of the molecule. In addition, the wall-to-wall separation is sufficiently large that contribution from the water inside the DNA grooves can be neglected. Thus treating the DNA in the B-phase as a solid rod (a common practice in biophysical research) is quite reasonable. In this model, the effective minimum separation is $d_w=d-d_B$, where d is the measured axial separation of DNA and d_B is the diameter of DNA in the B-form (d_B =20 Å).

In the A phase, the axial registration of the neighboring DNA molecules in the crystalline lattice "locks" the relative position of DNA helices with respect to each other and the molecules are in closer contact. Thus, the thickness of water layer is no longer just determined by the outer diameter of the A-DNA. One must take into account the water within the A-DNA double helix.

It is well established that the DNA double helix has major and minor grooves that can hold substantial amount of water (Egli et al., 1998; Guerri et al., 1998). We surmise that it is the locking of the relative positions of neighboring A-DNA molecules in the A phase that enabled

interpenetration. We can model the contribution of the water inside the grooves as having the effect of reducing the A-DNA diameter to $d'_A = d_A - \Delta d_w$, where $\Delta d_w = 2.4$ Å is the effective water layer thickness change during the B to A phase transition as derived from experimental data earlier. This value can also be estimated directly from structural parameters of A-DNA as follows. In the cross sectional view through the center of the c-axis, the A-DNA can be modeled as a rectangle with an unit area of $d_A P$, where d_A = 23 Å is the diameter of A-DNA and P =28 Å is the pitch. On this rectangle, we can approximate the major and minor grooves in A-DNA as having triangular profiles with depths and widths of d_M, W_M and d_m, W_m, respectively. The effective solid area of the A-DNA cross section can be derived by subtracting the area of the grooves:

$A = d_A P - d_M W_M - d_m W_m$

The effective solid rod diameter of the A-DNA is given by $A/P = d_A - (d_M W_M - d_m W_m)/P$. Correspondingly, one obtains $\Delta d_w = (d_M W_M - d_m W_m)/P$. Using the published parameters of A-DNA (major groove: depth 13.5 Å, width 2.7 Å; minor groove: depth 2.8 Å, width 11.0 Å) (Pattabhi, 2002), we arrive at a value for Δd_w = 2.41 Å, which matches the value derived from experimental data. Thus, the "effective diameter" of A-DNA becomes 20.6 Å for the purpose of deriving wall-to-wall separation in the A phase. It should be noted that the above calculation also confirms that the contribution from the narrow and deep major groove to the hydration force is rather small compared to the wide and shallow minor groove.

By applying different schemes as described above to derive the water layer thickness in the A and B phases, we arrive at a force-distance curve shown in Fig. 8. As expected, the A and B phase data points are essentially on a continuous line. Note that the surface separation d_w between DNA molecules varies from ~1.5 Å to 6 Å, a range unprobed by previous

measurements (Parsegian and Zemb, 2011). In the A and B co-existence regime the effective $d_{w\text{-}w}$ is calculated by $d_w = d-(w_A d_A + w_B d_B)$, where d_A and d_B are the effective diameters of A- (20.6Å) and B-DNA (20Å), respectively, and w_A and w_B are the corresponding phase fractions, which were calculated by comparing A- and B-DNA peak intensity values with diffraction data in the pure A- and B-DNA phases.

5. Materials & Methods

5.1 X-ray diffraction

For the experiments described in this paper, the H/T chamber was mounted on a motorized X-Y-Z sample stage which was fitted on a Huber 4-circle goniometer with a Rigaku rotating anode x-ray source (UltraX18HF, 0.3 mm point focus size). An Osmic™ confocal max flux multilayer monochromator was used to select Cu K_α radiation from the source and a MAR345 image plate detector was used to collect the diffraction data from the sample. The typical sample to detector distance is 18 cm, corresponding to a maximum scattering wave vector q_{max} of 3.0 $Å^{-1}$. Careful control of the incident beam divergence and profile by using a pair of slits allowed us to achieve a q_{min} of ~0.1 $Å^{-1}$, enabling both intermediate SAXS and WAXS studies on the same instrument.

5.2 DMPC lipid calibration sample preparation

The DMPC (Avanti Polar Lipids) was mixed with high resistivity water (18.2 MΩcm) to a ratio of 30 weight% water and 70 weight% DMPC. This mixture was spread over a heated ~5mm thick aluminum plate containing a 3 mm diameter hole; the plate was heated to a temperature to ensure that the DMPC solution would be in the L_α phase. The sample thickness was between 1 to 2 mm. Once this solution was set, the sample plate was mounted in the chamber, and the sample ambient environment was set to 37 °C, the dew point was set to 33 °C, and the sample

was left in the chamber to equilibrate for at least 12 hours. Subsequently, the sample temperature and relative humidity were set, and left to come to equilibrium (within 2 to 3 hours), and finally x-ray data was taken with an exposure time of two minutes.

5.3 DNA fiber preparation

The DNA solution used to draw the fibers consists of 40 weight% Calf Thymus DNA and 60 weight% buffer, a solution of 100 mM KCl in high resistivity (18.2 MΩcm) water. The mixture was placed in the cup of the fiber puller, and a fiber was initiated by dipping the pin into the cup containing the solution and pulling it up by hand. Once the fiber was initiated, the assembly was placed in an airtight cell in which the fiber could be elongated by drawing more solution at a controlled pulling speed of 100 μm per minute.

6. Conclusions

A unique design for a compact humidity and temperature controlled chamber suitable for in-situ x-ray scattering studies was presented. The H/T sample chamber was utilized to investigate the phase behavior of aligned DNA fibers as a function of hydration. The axial separation between DNA molecules was examined with consideration of structural differences in A and B conformations to generate a hydration force curve with an exponential decay length of ~2 Å, in good agreement with measurements by other methods. The results confirm that in the A-phase in which there is interpenetration of DNA helices the hydration force continues to play a dominant role in setting the DNA axial spacing.

Acknowledgements

Support for this work was provided by the U.S. Department of Energy (DOE), Office of

Basic Energy Sciences, Division of Materials Sciences and Engineering under award number DE-FG02-06ER46314 (force measurements of competing electrostatic and hydration interactions in DNA nanostructures) and the National Science Foundation under award numbers DMR-1401784 (DNA Phase Behavior). The research carried out here made extensive use of shared experimental facilities of the Materials Research Laboratory: an NSF MRSEC, supported by NSF DMR 1121053. *In this special contribution to the Festschrift in honor of D.L.D. Caspar, Y.L. would like to express deep gratitude to D.L.D. Caspar, as an inspirational Ph.D adviser and scientific mentor.*

REFERENCES

Atkins, P.W., 1994. Physical Chemistry, 5th ed. W.H. Freeman and Company, New York.

Banavali, N. and Roux, B., 2005. Free Energy Landscape of A-DNA to B-DNA Conversion in Aqueous Solutions. J. Am. Chem. Soc. 127, 6866-6876.

Berg, J.M, Tymoczko, J.L., and Stryer, L., 2002. Biochemistry, 5th Ed., W.H. Freeman, New York.

Blanc, N.S., Senn, A., Loforestier, A., Livolant, F., Dubochet, J., 2001. DNA in human and stallion spermatozoa forms local hexagonal packing with twist and many defects. J. Struct. Biol. 134, 76-81.

Chaplin, M., 2006. Nat. Rev. 7, 861-866.

van Dam, L., Korolev, N., Nordenskiöld, L., 2002. Polyamine-nucleic acid interactions and the effects on structure in oriented DNA fibers. Nucleic Acids Res. 30, 419-428.

Dickerson, R.E. and Ng H.L., 2001. DNA structure from A to B. Proc. Natl. Acad. Sci. USA 98, 6986-6988.

Durand, D., Doucet, J., Livolant, F., 1992. A study of the structure of highly concentrated phases of DNA by X-ray diffraction. J. De Phys. II. 2, 1769 – 1783.

Egli, M., Tereshko, V., Teplova, M., Minasov, G., Joachimiak, A., Sanishvili, R., Weeks, C.M., Miller, R., Maier, M.A., An, H., Cook, P.D., Manoharan, M., 1998. X-Ray Crystallographic Analysis of the Hydration of A- and B-Form DNA at Atomic Resolution. Biopolymers (Nucleic Acid Sciences) 48, 234-252.

Fuller, W., Forsyth, T. and Mahendrasingam, A., 2004. Water-DNA interaction as studied by x-ray and neutron fibre diffraction. Philosophical Transactions: Biological Sciences (Royal Society) 359, No 1449, 1237-1278.

Fuller, W., Wilkins, M.H.F., Wilson, H.R. and Hamilton, L.D., 1965. The Molecular Configuration of Deoxyribonucleic Acid IV. X-ray Diffraction Study of the A Form. J. Mol. Biol. 12, 60-80.

Franklin, R.E., Gosling, R.G., 1953a. The Structure of Sodium Thymonucleate Fibres. I. The Influence of Water Content. Acta Cryst. 6, 673-677.

Franklin, R.E., Gosling, R.G., 1953b. Molecular configuration in Sodium Thymonucleate. Nat. 171, 740-741.

Guirri, A., Simpson, I.J. and Neidle, S., 1998. Visualization of extensive water ribbons and networks in a DNA minor-groove drug complex. Nucl. Acid. Res. 26, 2873-2878.

Haar, L., Gallagher, J.S., Kell, G.S., 1984. Handbook of Chemistry and Physics, 84th ed. pp. 6-8. *NBS/NRC Steam Tables*. Hemisphere Publishing Corp., New York.

Langridge, R., Wilson, H.R., Hooper, C.W., Wilkins, M.H.F., Hamilton, L.D., 1960. The molecular configuration of deoxyribonucleic acid: I. X-ray diffraction study of a crystalline form of the lithium salt. J. Mol. Biol. 2, 19-37.

Leikin, S., Pargegian, V.A., Rau, D.C., Rand, R.P., 1993. Hydration Forces. Annu. Rev. Phys. Chem. 44, 369-395.

Livolant, F., 1991a. Supramolecular organization of double-stranded DNA molecules in the columnar hexagonal liquid crystalline phase: An electron microscopic analysis using freeze-fracture methods. J. Mol. Biol. 218, 165-181.

Livolant, F., 1991b. Ordered phases of DNA in vivo and in vitro. Physica A. 176, 117-137.

Livolant, F., Lecelut, A.M., Doucet, J., Benoit, J.P., 1989. The highly concentrated liquid-crystalline phase of DNA is columnar hexagonal. Nat. 339, 724-726.

Livolant, F.,Leforestier, A., 1996. Condensed phases of DNA: Structures and phase transactions. Prog. in Polym. Science 21, 1115-1164.

Mitsui, Y., Langridge, R., Shortle, B.E., Cantor, C.R., Grant, R.C., Kodoma, M. & Wells, R.D., 1970. Physical and Enzymatic Studies on Poly d(I-C).Poly d(I-C), an Unusual Double Helical DNA. Nature, 228, 1166-1169.

Parsegian, V.A., Fuller, N., and Rand, R.P., 1979. Measured work of deformation and repulsion of lecithin bilayers. Proc. Natl., Acad. Sci. USA 76, 2750-2754.

Parsegian, V.A., Zemb, T., 2011. Hydration forces: Observations, explanations, expectations and questions. Curr. Op. Coll. & Int. Sci. 16, 618-624.

Pattabhi, V., Gautham, N., 2002. Biophysics. Pg. 151. Alpha Sciences Int., Pangbourne, U.K.

Podgornik, R., Rau, D.C., Parsegian, V.A., 1994. Parameterization of direct and soft steric-undulatory forces between DNA double helical polyelectrolytes in solutions of several different anions and cations. Biophys. J. 66, 962-971.

Rau, D.C., Lee, B. and Pargegian, V.A., 1984. Measurement of the repulsive force between polyelectrolyte molecules in ionic solution: Hydration forces between parallel DNA double helices. Proc. Natl. Acad. Sci. USA 81, 2621-2625.

Rau, D.C. and Parsegian, V.A., 1992. Direct measurement of temperature-dependent solvation forces between DNA double helices. Biophys. J. 61, 260-271.

Safinya, C. R.; Clark, N. A.; Liang, K. S.; Varady, W. A.; Chiang, L. Y., 1985. Synchrotron X-ray Scattering Study of Freely Suspended Discotic Strands. Mol. Cryst. Liq. Cryst. 123, 205-216.

Safinya, C. R.; Liang, K. S.; Varady, W. A.; Chiang, L. Y., 1984. Synchroton X-ray Study of the Orientational Ordering D2-D1 Structural Phase Transition of Freely Suspended Discotic Strands in Triphenylene-Hexa-dodecanoate. Phys. Rev. Lett. 53, 1172-1175.

Sirota, E.B., Smith, G.S., Safinya, C.R., Plano, R.J., Clark, N.A., 1988. X-ray Scattering Studies of Aligned Stacked Surfactant Membranes. Science. 242, 1406-1409.

Sirota, E.B., Wu, X.Z., 1996. The rotator phases of neat and hydrated 1-alcohols. J. Chem. Phys. 105, 7763-7773.

Smith, G.S., Sirota, E.B., Safinya, C.R., Plano, R.J., Clark, N.A., 1990. X-ray structure studies of freely suspended ordered hydrated DMPC multimembrane films. J. Chem. Phys. 92, 4519-4529.

Smith, G.S., Sirota, E.B., Safinya, C.R., Plano, R.J., Clark, N.A., 1988. Structure of the L_{β}' Phase in a Hydrated Phosphatidylcholine Multimembrane. Phys. Rev. Lett. 60, 813-816. \

Watson, J.D. and Crick, F.H.C., 1953. A Structure for Deoxyribose Nucleic Acid. Nature 171, 737-738.

.

FIGURE CAPTIONS

Fig. 1 Operating principle of the differential temperature control humidity chamber. (a) The relative humidity is derived based on the partial vapor pressure at the sample held at a temperature at or above the water reservoir temperature, which sets the dew point of the sample environment. (b) Fit to tabulated water vapor pressure values. The Clausius-Clapeyron Equation was used to fit data taken from published tabulated data (Haar et al., 1984). (c) Calculated range of temperature and humidity values that can be achieved with the sample chamber.

Fig. 2 Mechanical design and control diagram of the humidity temperature chamber**.** (a) The assembly consists of three concentric cylinders (only the two inner shells are shown). The outer insulating case is used to improve temperature stability against ambient fluctuations. (b) The temperature of the sample is set by controlling the temperature of the outer aluminum cylinder, and the relative humidity at the sample position is set by controlling the dew point at the sample via the temperature of the reservoir. Resistive heaters are placed on the middle aluminum cylinder to enhance temperature stability, and the layer of air between this and the innermost cylinder surrounding the sample dampens temperature fluctuations.

Fig. 3 Results of calibration experiments using the phase transition of a lyotropic DMPC/water sample. (a,b) 2D X-ray diffraction patterns of a DMPC membrane sample taken at constant temperature (36.6 ºC) with different relative humidity (70.4% RH for (a) and 69.4% RH for (b)). The sharpening of the in-plane diffraction arc in (b) indicates ordering of the lipid tails. (c,d). Schematic illustrations of molecular organizations of the lipid membrane in the L_{α} (c) and $L_{\beta f}$ phases (d), respectively. (e). Meridional (Z axis) intensity profiles of the 2D diffraction data,

representing lamellar stacking order of the lipid bilayer membrane. (f). Equatorial (X axis) intensity profiles of the 2D diffraction data, showing the transition from L_α τo $L_{\beta f}$ phase.

Fig. 4 Automated DNA strand puller for the humidity/temperature chamber. (a) The sealed miniature fiber puller with stepper motor for pulling DNA fibers at a controlled rate. (b,c). Polarized microscopy images of a DNA fiber sample showing the aligned domains in the sample (The fiber sample was rotated by 45 degrees between b and c).

Fig. 5 In-situ 2D x-ray diffraction data collected at different relative humidity levels from an aligned DNA fiber sample using the H/T chamber at T=30 ^{o}C. The top four panels show characteristic features of the B-form DNA whereas the bottom panels at lower humidity are in mixed B+A or pure A-form as indicated.

Fig. 6 Conversion of B-DNA to A-DNA driven by reduced humidity. (a) Pitch of DNA double helix as a function of humidity showing the transition from B- to A-form starting at RH ~87%. Between RH ~82% - 87% (dashed vertical lines) there is coexistence of A- and B-forms. Error bars for RH were determined by propagating thermistor uncertainties through the Claussius-Clapeyron equation while uncertainties in pitch were determined by calculating the detector's q_z resolution at the first and second layer lines of B- and A-DNA respectively. (b) Intensity profiles of the first equatorial peak in the humidity range of pure B-DNA, to a coexistence of B- and A-DNA, and finally to pure A-DNA. In the co-existence range (between RH 83%-87%) the peak position (hence interhelical separation) remains unchanged (vertical line).

Fig. 7 The dependence of inter-helical spacing on the log of the differential pressure exerted on the DNA molecules. The pressure is directly related to change in the chemical potential due to relative humidity. The linear correlation exhibited in both phases confirms the characteristic exponential dependence of hydration force on separation distance, with a decay length of $\lambda \sim 2$Å.

Fig.8 The hydration force curve for both A and B phases. In the B-DNA phase, the wall-to-wall separation (minimum water layer thickness) is derived by subtracting the diameter of B-DNA (20 Å) from the interhelical spacing. In the A-DNA phase, *dw* is derived by first subtracting the diameter of A-DNA (23 Å), then adding 2.4 Å to account for the contribution from water within the major and minor grooves in A-DNA. In the A and B co-existence regime the effective d_w is calculated by $d_w = d-(w_A d_A + w_B d_B)$, where d_A and d_B are the effective diameters of A- (20.6Å) and B-DNA (20Å), respectively, and w_A and w_B are the corresponding phase fractions.

Figure 1
Click here to download high resolution image

Figure 1

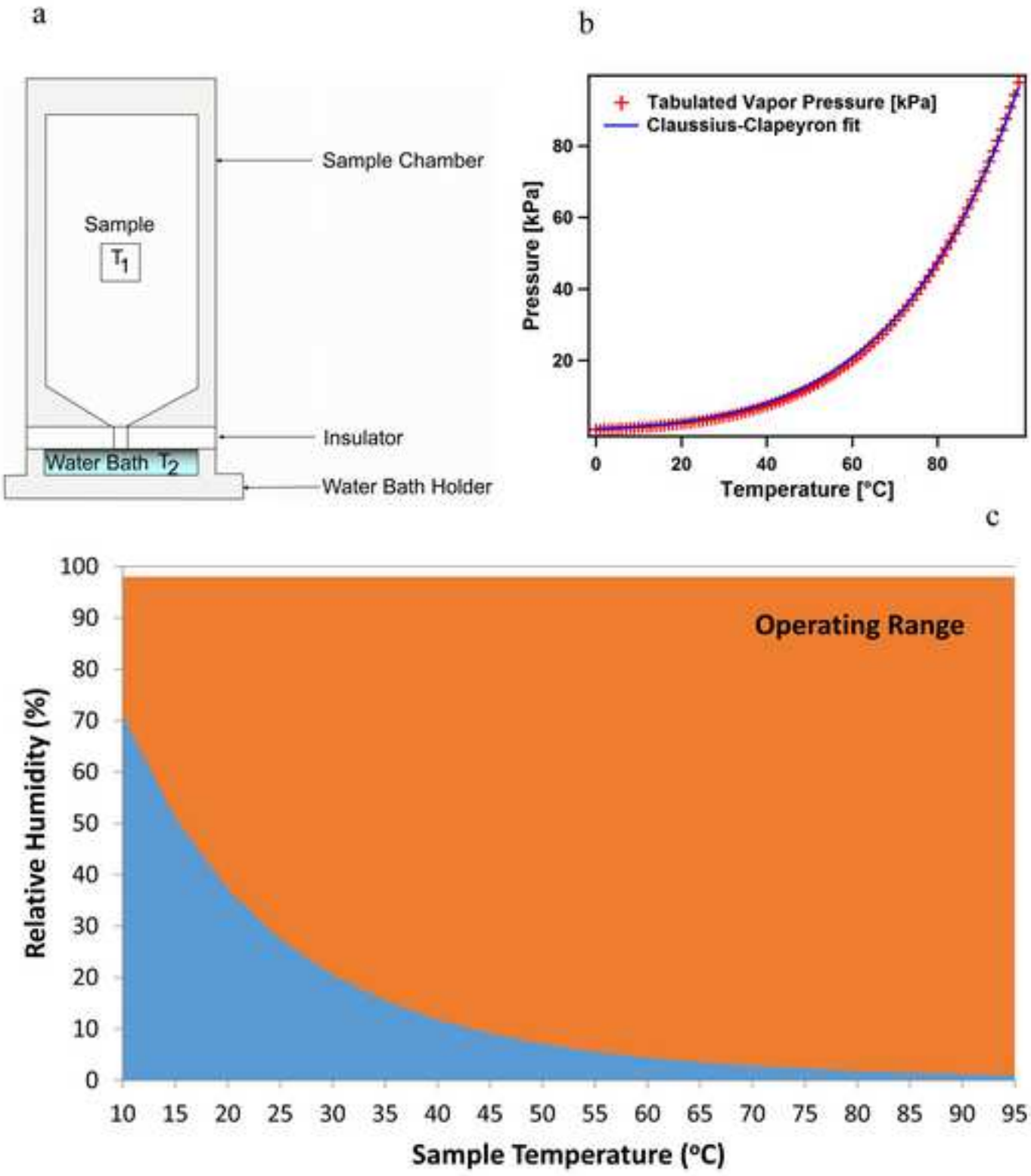

Figure 2

Click here to download high resolution image

Figure 2

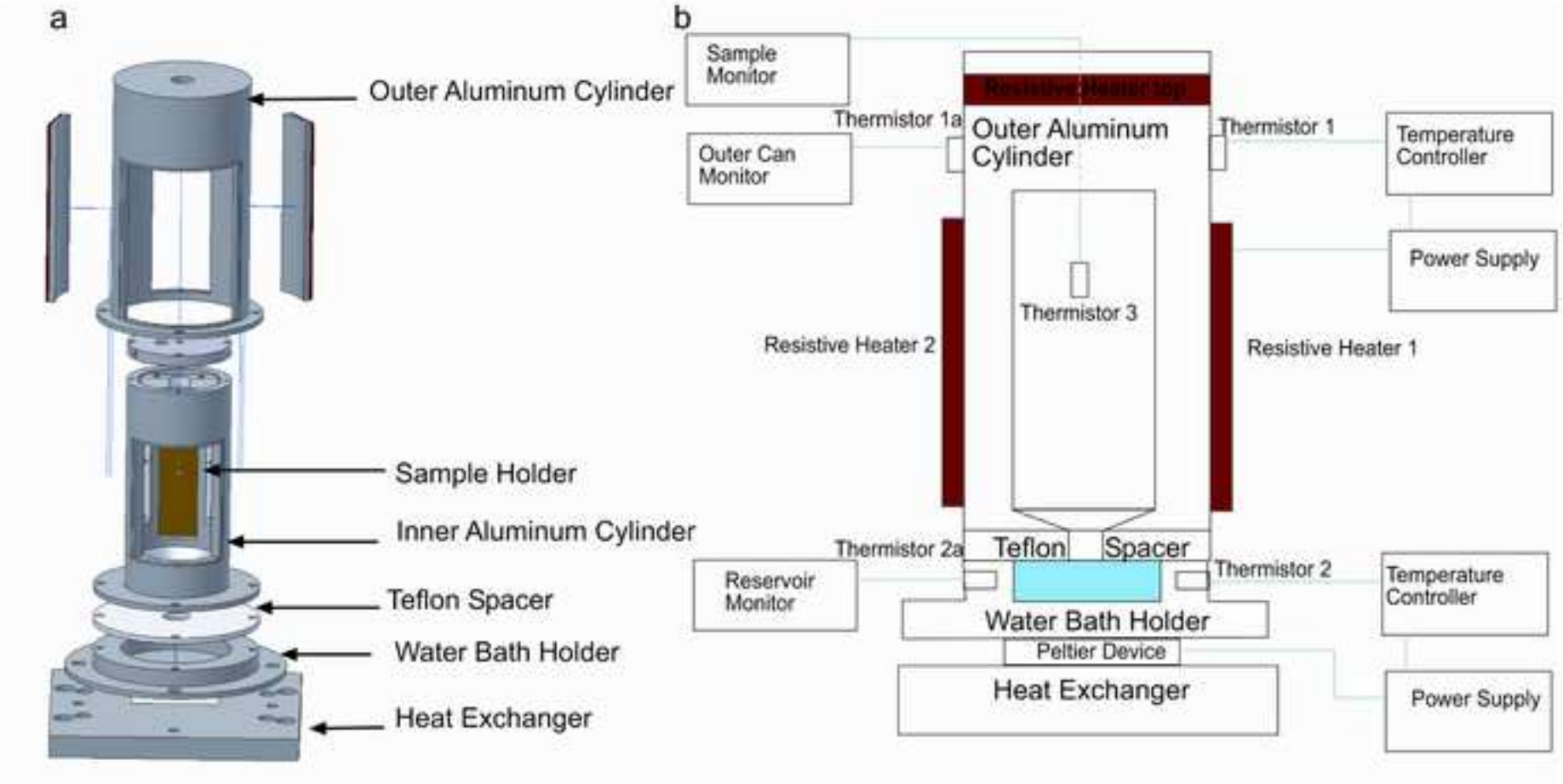

Figure 3

Click here to download high resolution image

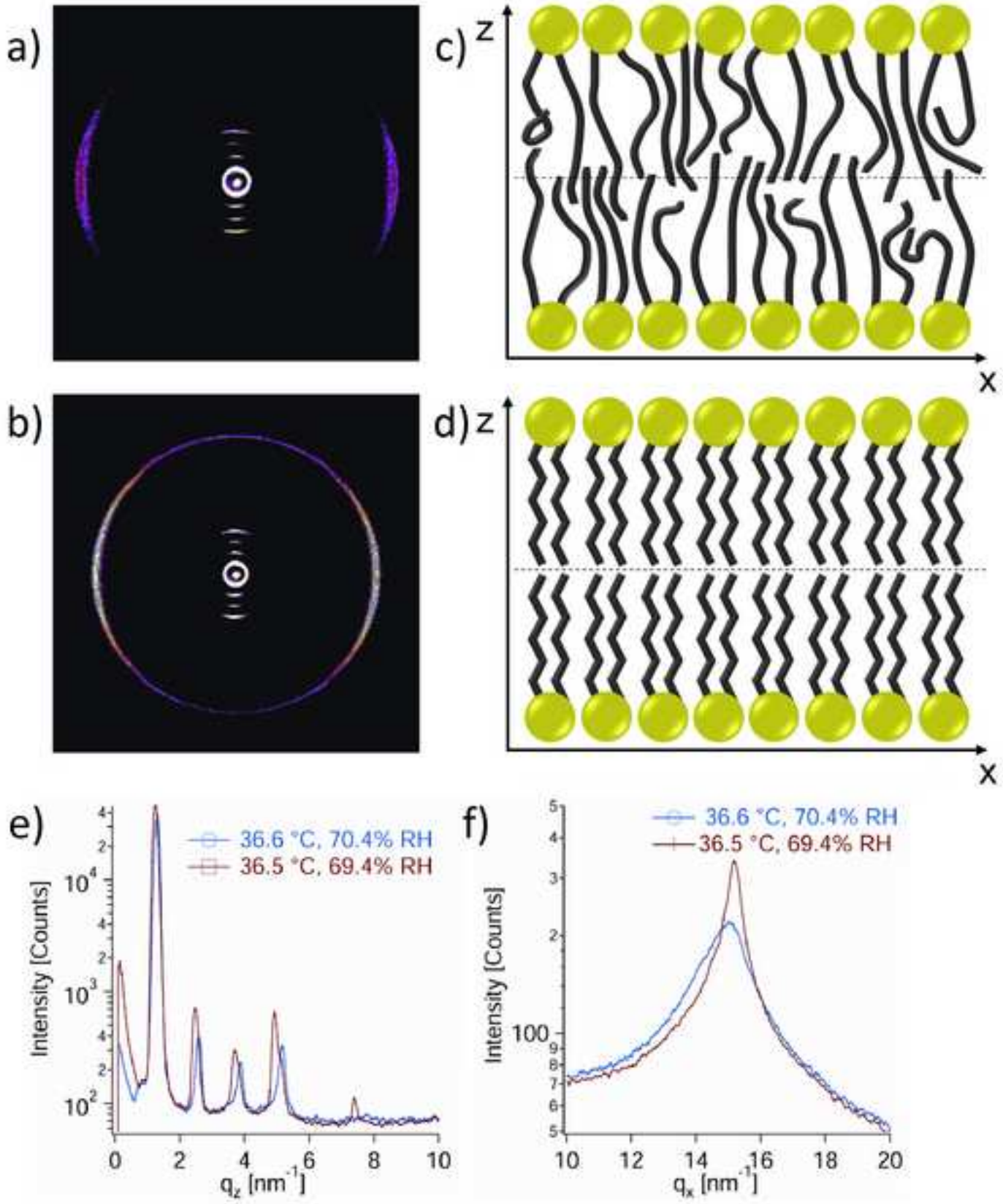

Figure 4

Click here to download high resolution image

Figure 4

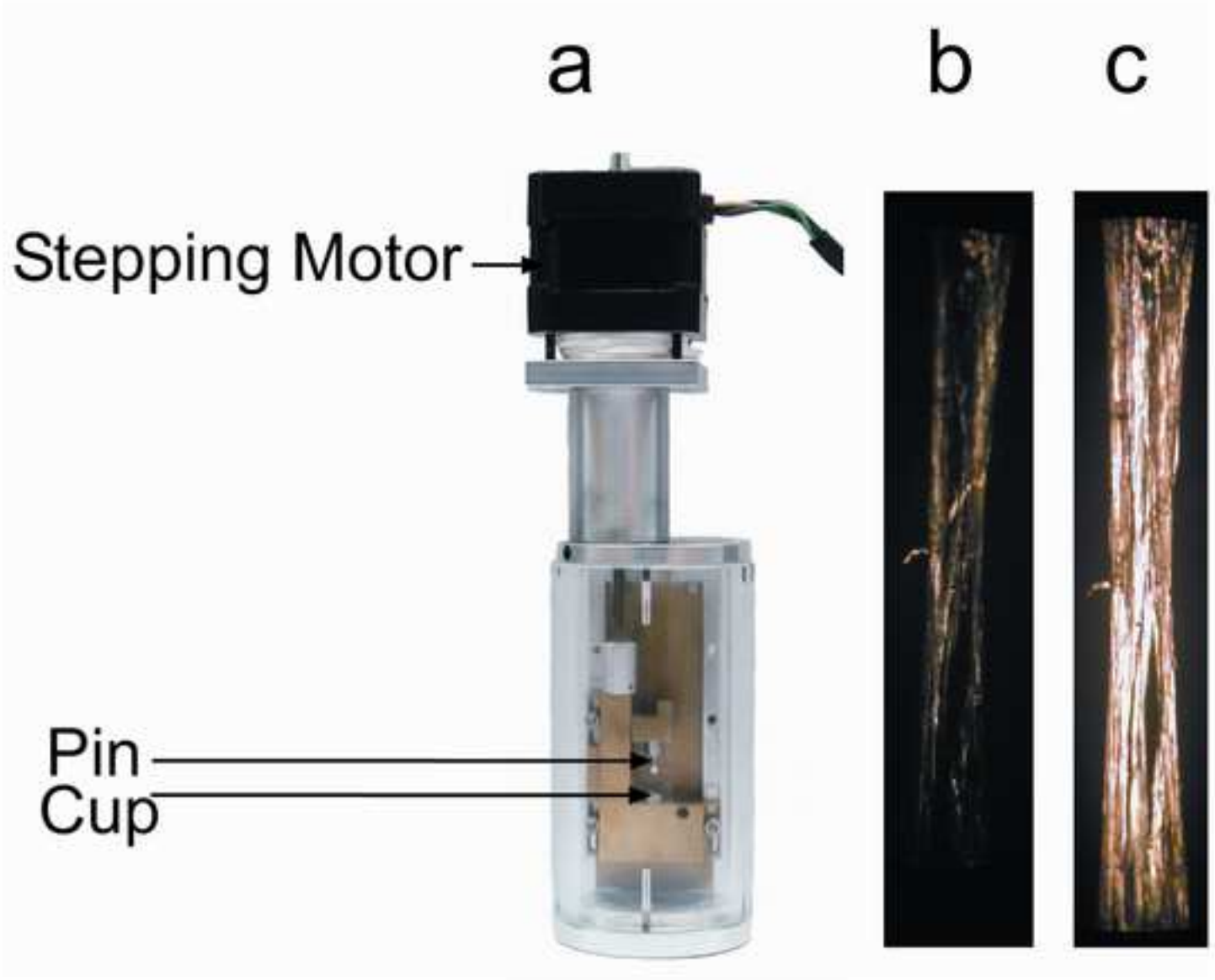

Figure 5
Click here to download high resolution image

Figure 5

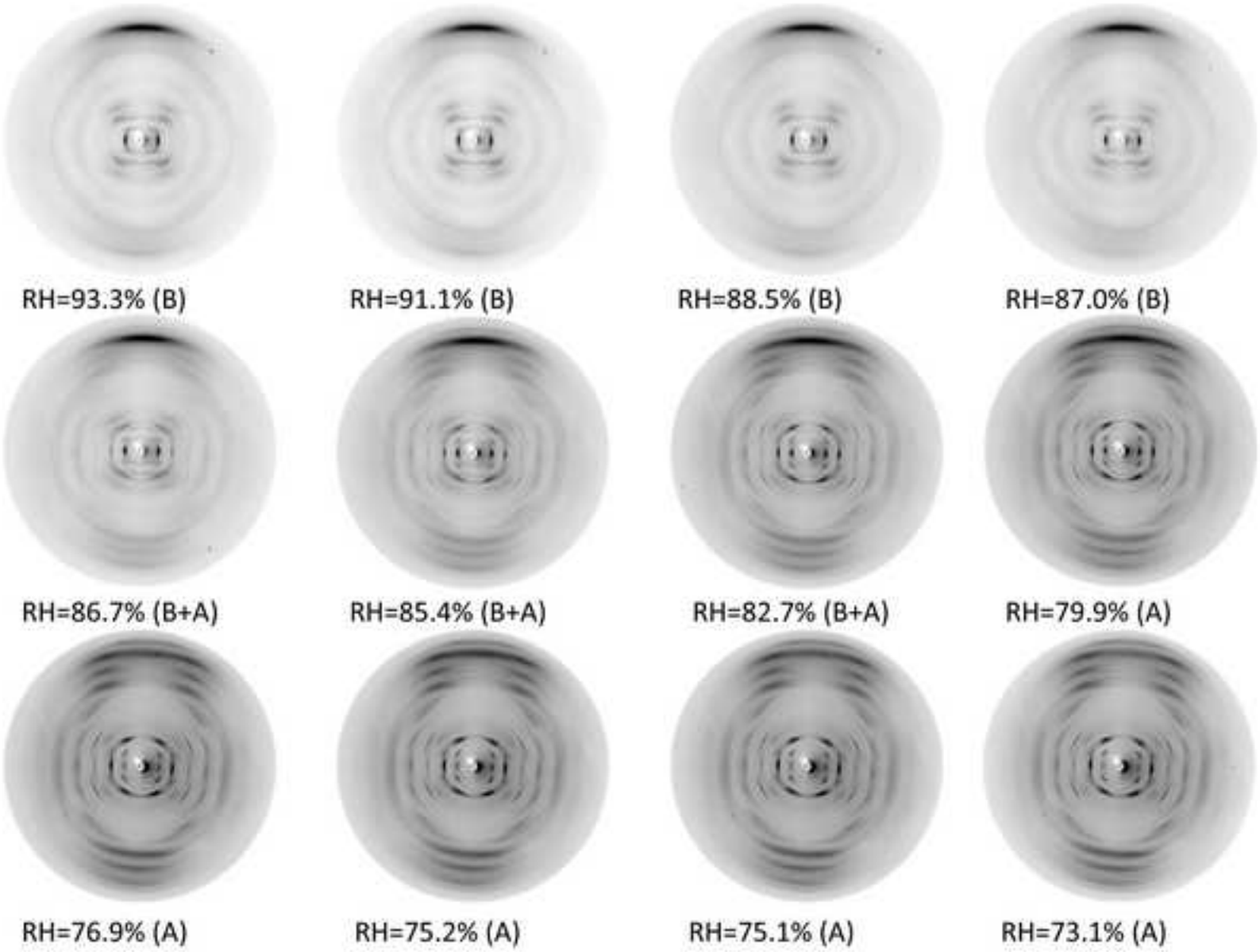

Figure 6

Click here to download high resolution image

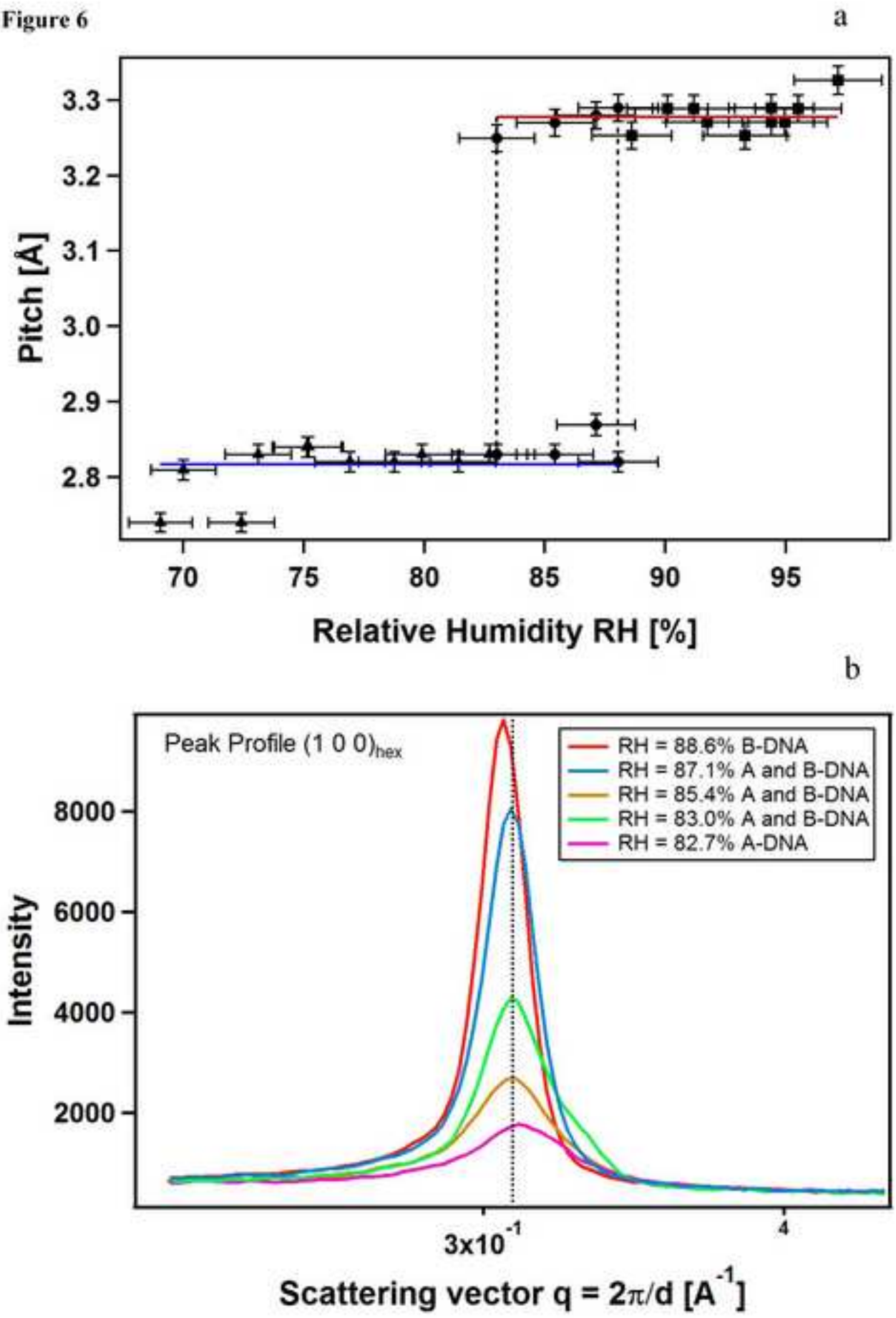

Figure 7

Click here to download high resolution image

Figure 7

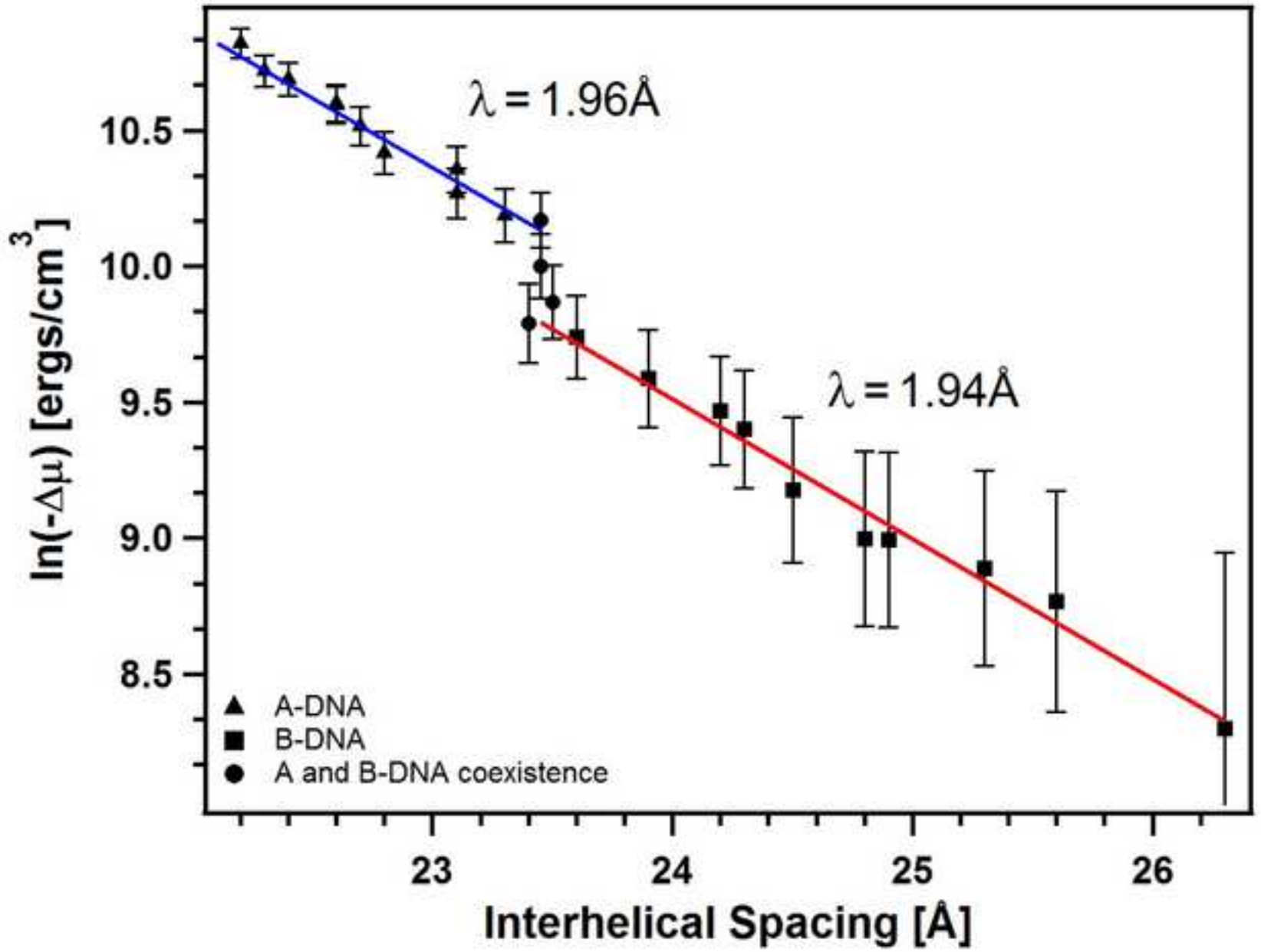

Figure 8

Click here to download high resolution image

Figure 8